中国光学（中英文） Chinese Optics 核心期刊

Multi-objective parameter optimization of abrasive water jet polishing for fused silica

LI Qian, YAO Peng, DENG Hong-xing, FENG Chen-yu, XU Chong-hai, QU Shuo-shuo, YANG Yu-ying, ZHU Hong-tao, HUANG Chuan-zhen

Citation:
LI Qian, YAO Peng, DENG Hong-xing, FENG Chen-yu, XU Chong-hai, QU Shuo-shuo, YANG Yu-ying, ZHU Hong-tao, HUANG Chuan-zhen. Multi-objective parameter optimization of abrasive water jet polishing for fused silica[J]. *Chinese Optics*, 2025, 18(5): 1185-1199. doi: 10.37188/CO.EN-2025-0006
李倩, 姚鹏, 邓红星, 冯辰宇, 许崇海, 屈硕硕, 杨玉莹, 朱洪涛, 黄传真. 磨料水射流抛光熔石英玻璃的多目标参数优化[J]. 中国光学, 2025, 18(5): 1185-1199. doi: 10.37188/CO.EN-2025-0006

View online: https://doi.org/10.37188/CO.EN-2025-0006

Articles you may be interested in

Isolation of single wavelength laser communication terminals
单波长激光通信终端的隔离度
Chinese Optics. 2023, 16(5): 1137 https://doi.org/10.37188/CO.2022-0253

Light modulation performance control of the coating on the repaired damage sites in fused silica surface
膜层对熔石英表面损伤修复点光调制性能调控研究
Chinese Optics. 2021, 14(3): 552 https://doi.org/10.37188/CO.2020-0110

Research progress of elastic emission machining in optical manufacturing
弹性发射光学制造技术研究进展
Chinese Optics. 2021, 14(5): 1089 https://doi.org/10.37188/CO.2021-0022

Progress on defect and related carrier dynamics in two-dimensional transition metal chalcogenides
二维过渡金属硫族化合物中的缺陷和相关载流子动力学的研究进展
Chinese Optics. 2021, 14(1): 18 https://doi.org/10.37188/CO.2020-0106

Spectral diagnosis of an arc jet actuator
电弧射流激励器光谱诊断研究
Chinese Optics. 2023, 16(2): 296 https://doi.org/10.37188/CO.2022-0097

Establishment and analysis of the diffraction bidirectional reflection distribution function model for surface defects
表面损伤衍射双向反射分布函数模型建立及分析
Chinese Optics. 2021, 14(2): 375 https://doi.org/10.37188/CO.2020-0162

文章编号 2097-1842(2025)05-1185-15

Multi-objective parameter optimization of abrasive water jet polishing for fused silica

LI Qian[1,2,3], YAO Peng[2,3*], DENG Hong-xing[2,3], FENG Chen-yu[2,3], XU Chong-hai[1], QU Shuo-shuo[2,3], YANG Yu-ying[1], ZHU Hong-tao[2,3], HUANG Chuan-zhen[4]

(1. *School of Mechanical Engineering*, *Qilu University of Technology (Shandong Academy of Sciences)*, *Jinan* 250353, *China*;

2. *Center for Advanced Jet Engineering Technologies (CaJET)*, *School of Mechanical Engineering*, *Shandong University*, *Jinan* 250061, *China*;

3. *Key Laboratory of High Efficiency and Clean Mechanical Manufacture*, *Ministry of Education*, *Shandong University*, *Jinan* 250061, *China*;

4. *School of Mechanical Engineering*, *Yanshan University*, *Qinhuangdao* 066004, *China*)

* *Corresponding author*, *E-mail*: *yaopeng@sdu.edu.cn*

Abstract: As a non-contact ultra-precision machining method, abrasive water jet polishing (AWJP) has significant application in optical elements processing due to its stable tool influence function (TIF), no subsurface damage and strong adaptability to workpiece shapes. In this study, the effects of jet pressure, nozzle diameter and impinging angle on the distribution of pressure, velocity and wall shear stress in the polishing flow field were systematically analyzed by computational fluid dynamics (CFD) simulation. Based on the Box-Behnken experimental design, a response surface regression model was constructed to investigate the influence mechanism of process parameters on material removal rate (MRR) and surface roughness (Ra) of fused silica. And experimental results showed that increasing jet pressure and nozzle diameter significantly improved MRR, consistent with shear stress distribution revealed by CFD simulations. However, increasing jet pressure and impinging angle caused higher Ra values, which was unfavorable for surface quality improvement. Genetic algorithm (GA) was used for multi-objective optimization to establish Pareto solutions, achieving concurrent optimization of polishing efficiency and surface quality. A parameter combination of 2 MPa jet pressure, 0.3 mm nozzle diameter, and 30° impinging angle achieved MRR of 169.05 μm³/s and Ra of 0.50 nm. Experimental verification showed prediction errors of 4.4% (MRR) and 3.8% (Ra), confirming the model's reliability. This parameter optimization system provides theoretical basis and technical support for ultra-precision polishing of complex curved optical components.

收稿日期:2025-02-08; **修订日期**:2025-03-10

基金项目:国家重点研发计划项目(No. 2023YFC2413301);国家自然科学基金区域联合基金重点项目(No. U23A20632);山东省自然科学基金重大基础研究项目(No. ZR2023ZD34)

Supported by National Key Research and Development Program of China (No. 2023YFC2413301); National Natural Science Foundation of China (No. U23A20632); Major Basic Research of Shandong Provincial Natural Science Foundation (No. ZR2023ZD34)

Key words: abrasive; computational fluid dynamics; tool influence function; material removal rate; surface roughness

磨料水射流抛光熔石英玻璃的多目标参数优化

李　倩[1,2,3], 姚　鹏[2,3]*, 邓红星[2,3], 冯辰宇[2,3], 许崇海[1], 屈硕硕[2,3], 杨玉莹[1], 朱洪涛[2,3], 黄传真[4]

（1. 齐鲁工业大学 (山东省科学院) 机械工程学部, 山东 济南 250353;
2. 山东大学 机械工程学院 先进射流工程技术研究中心, 山东 济南 250061;
3. 山东大学 机械工程学院 高效洁净机械制造教育部重点实验室, 山东 济南 250061;
4. 燕山大学 机械工程学院, 河北 秦皇岛 066004）

摘要: 磨料水射流抛光技术作为一种非接触式超精密加工方法, 因其材料去除函数稳定、无亚表面损伤及强形状适应性, 在光学元件加工领域具有重要应用价值。本研究通过计算流体动力学(CFD)数值模拟方法, 系统分析了射流压力、喷嘴直径及入射角度对抛光流场压力分布、速度分布及壁面剪切力分布的作用规律。基于 Box-Behnken 实验设计, 构建了响应面回归模型, 系统研究了工艺参数对熔石英玻璃的材料去除率(MRR)和表面粗糙度(Ra)的影响机制。实验结果表明: 通过增大射流压力和喷嘴直径可显著提高 MRR, 该规律与流场仿真揭示的剪切应力分布特征一致; 但增大射流压力和入射角度会导致 Ra 增大, 不利于表面质量提升。通过遗传算法(GA)多目标优化建立 Pareto 解集, 成功实现了加工效率与表面质量的协同优化, 在射流压力为 2 MPa、喷嘴直径为 0.3mm、入射角度为 30°的参数组合下 MRR 达 169.05 μm³/s、Ra 低至 0.50 nm。实验结果表明, 模型预测值与实测值误差仅为 4.4%(MRR)和 3.8%(Ra), 验证了模型的可靠性。本研究建立的参数优化体系为复杂曲面光学元件的超精密抛光提供了理论依据与技术支持。

关　键　词: 磨粒; 计算流体动力学; 去除函数; 材料去除率; 表面粗糙度

中图分类号: TH162　　**文献标志码:** A　　**doi:** 10.37188/CO.EN-2025-0006　　**CSTR:** 32171.14.CO.EN-2025-0006

1 Introduction

Fused silica is characterized by space stability, high hardness, high surface finish and excellent thermal stability. It has been widely used in aerospace, optical systems, electronic equipment, defense technology and other fields[1-3]. The ultra-precision machining of optical glass with high efficiency and low damage has attracted considerable attention from researchers in recent years[4]. However, due to the high brittleness and low fracture toughness of optical glass, brittle fracture is inevitably generated during processing, which affects its ultimate performance[5]. Therefore, there is an urgent need for high-performance and deterministic polishing techniques to manufacture these high-value and challenging optical surfaces, and to meet their demanding processing requirements, including excellent surface quality, low cost, and high efficiency[6]. As a promising ultra-precision deterministic polishing technique, abrasive water jet polishing (AWJP) distinguishes itself through high polishing precision, non-destructive subsurface integrity, geometric adaptability for complex profiles, stable localized tool influence function (TIF), and broad material applicability. However, its material removal rate (MRR) remains lower than hybrid processes. These attributes enable AWJP to address challenges in machining complex surfaces and other optical components fabricated from difficult-to-process materials[7-11].

AWJP, initially proposed by Faehnle *et al*.. realized material removal by the combined action of abrasive particle impacts and hydrodynamic shear forces, and the material removal characterization and experimental optimization of optical lenses were also investigated[12–15]. The polishing effect is

affected by many factors, including jet pressure, impinging angle, polishing duration, and abrasive slurry concentration. Renowned for its stable and small tool influence function (TIF), absence of subsurface damage, high precision material removal, and boundary-free processing capability[16–19], AWJP has been widely applied to optical elements with planar, aspherical, and free-form surfaces, etc. At the same time, it also has the modification ability in the polishing process, which can meet the processing requirements of high surface shape accuracy and low surface roughness (Ra) of nonlinear complex surfaces. Extensive experimental investigations have been conducted to characterize the effects of process parameters on surface generation. Zhu *et al*.. systematically analyzed the ductile erosion mechanisms in AWJP of hard-brittle materials under small impinging angles[20]. Matsumura *et al*.. performed AWJP on glass chips to eliminate the effects of milling marks and subsurface damage after micro-milling machining, which reduced the Ra to 25 nm[21]. Li *et al*.. demonstrated effective removal of diamond turning marks on electroless nickel mirrors, achieving Ra improvements from 400 nm to 4 nm (rough samples) and 3.7 nm to 1.4 nm (fine samples)[22]. Tsai *et al*.. optimized AWJP parameters for SKD61 die steel using Taguchi methods, achieving an 87% reduction in Ra[23]. Wang *et al*.. developed a novel multi-jet polishing system that significantly improved material removal efficiency through enhanced surface coverage[24]. Kumaran *et al*.. established regression models to predict Ra based on input parameters, identifying critical factors affecting surface quality[25]. Cao *et al*.. combined Taguchi experiments and computational fluid dynamics (CFD) simulations to develop erosion models for BK7 optical glass[26]. Zhang *et al*.. proposed a hybrid model integrating CFD and kinetic analysis to predict MRR at different jet pressures, providing a theoretical basis for deterministic polishing control[27].

However, current AWJP research has primarily focused on single-parameter optimization, lacking systematic investigation into multi-parameter interactions. Although empirical models link single parameters to surface quality, the interactions among jet pressure, nozzle diameter, and impinging angle remain poorly understood. Traditional empirical models fail to predict parameter interactions affecting both MRR and Ra, which are inherently conflicting objectives in ultra-precision polishing. This study bridges this gap by using CFD to analyze flow fields and Box-Behnken experimental design (BBD) to quantify parameter interactions and construct a second-order response surface regression model. The model quantifies the interactive effects of process parameters on MRR and Ra, providing a predictive framework for multi-objective optimization. By integrating genetic algorithm (GA) optimization, Pareto optimal solutions balancing MRR and Ra objectives are derived, thereby enabling deterministic ultra-precision polishing of fused silica.

2 Experimental investigation

2.1 Experimental setup

The AWJP technology achieves material removal and surface finishing of optical elements through the normal impact stresses and tangential shear stresses exerted by abrasive water slurry jet. The fundamental principle of its polishing is illustrated in Fig. 1 (color online). In the slurry tank, abrasives are thoroughly mixed with water through mechanical agitation. The resultant slurry is pumped to the nozzle, forming a high-velocity jet beam[28]. The slurry jet is then directed onto the workpiece surface at a specific velocity to achieve material removal. Following processing, the spent polishing fluid is recirculated to the slurry tank for recycling. The experiment is carried out on the machine shown in Fig. 2, which provides *X*, *Y*, and *Z* linear motion capabilities. The slurry nozzle is vertically mounted on the *Z*-axis with adjustable angle. The machine drives the nozzle to reciprocate parallel to the *X*-

axis, performing 5-mm linear polishing on fused silica.

To ensure TIF stability, polishing slurry homogeneity was maintained through dispersant and suspending agent addition combined with continuous stirring, complemented by regular replacement to prevent particle sedimentation. A precision filter at the pump inlet minimized contamination risks, while high-pressure water tubing and sealed fittings preserved system integrity. Pressure stability was ensured via an integrated accumulator, complemented by real-time digital monitoring for process consistency.

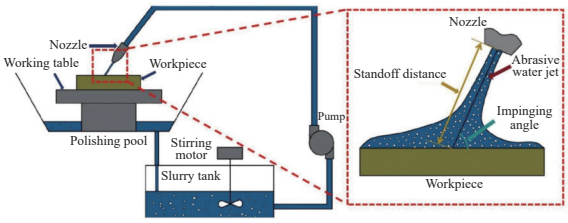

Fig. 1 Schematic diagram of AWJP

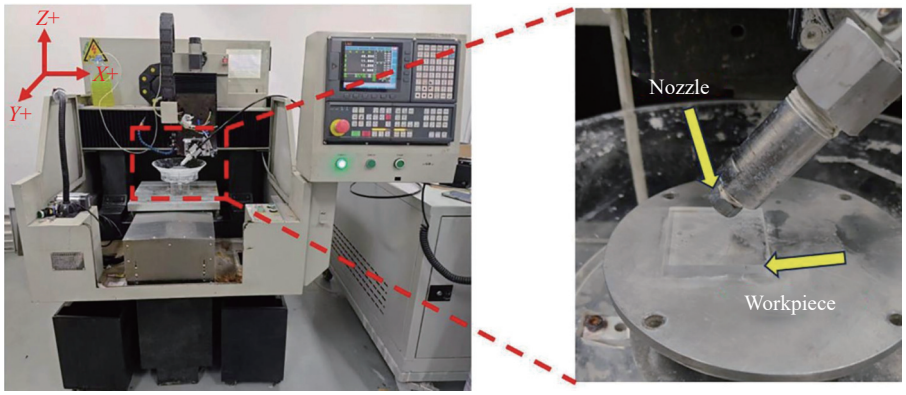

Fig. 2 Experimental setup

2.2 Experimental design

Previous studies have demonstrated that jet pressure, nozzle diameter, and impinging angle significantly influence AWJP surface quality[29-31]. To model factor interactions and optimize parameters, the response surface methodology (RSM) with BBD was employed, followed by GA optimization. The experimental factor levels are detailed in Table 1.

Tab. 1 AWJP parameters

levels	Jet pressure (MPa)	Nozzle diameter (mm)	Impinging angle (°)
−1	2	0.3	30
0	3	0.5	45
1	4	0.7	60

CeO_2 abrasives with an average particle size of 1 μm were used. The scanning electron microscope (SEM) image in Fig. 3 shows irregular CeO_2 particles with uniform size distribution. A 6 wt.% CeO_2 polishing slurry was prepared by mixing deionized water, dispersant, and suspending agent[32].

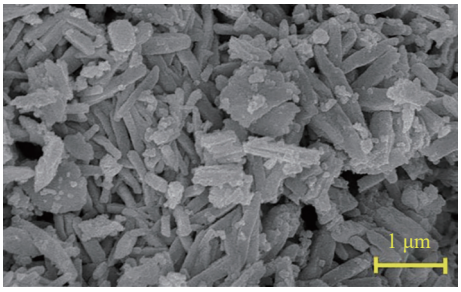

Fig. 3 The SEM image of CeO_2 abrasive

To ensure experimental consistency, critical process parameters were standardized as follows: nozzle-to-workpiece standoff distance = 10 mm, nozzle feed rate = 200 mm/min, and single-pass polishing duration = 10 min. Surface topography characterization employed a SuperView WX120 white light interferometer to quantify three-dimensional morphology evolution and TIF characteristics, as illustrated in Fig. 4 (color online). Surface topography of the polished workpiece is presented in Fig. 5 (color online).

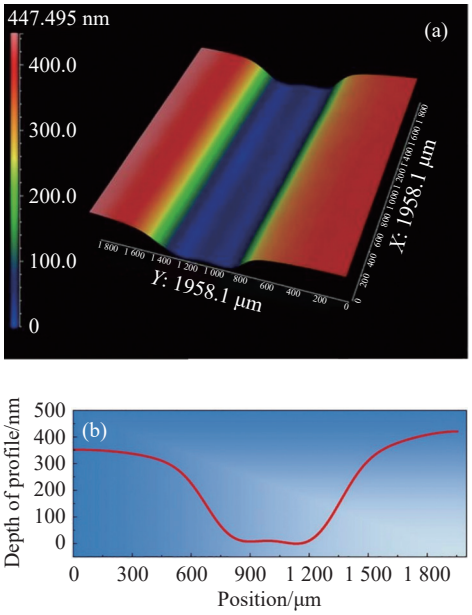

Fig. 4　The white light 3D interferometer image of (a) the removal profile and (b) cross-sectional TIF

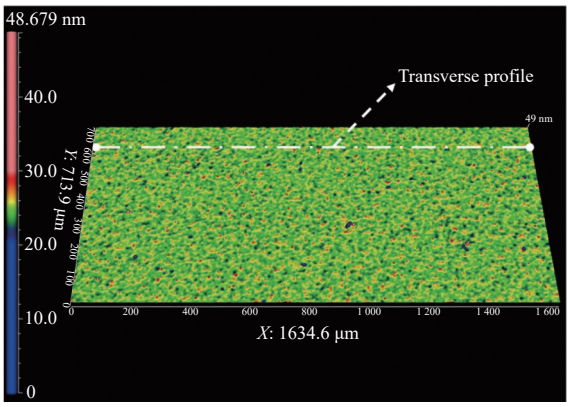

Fig. 5　Polished surface topography observed via white light interferometry

Ra measurements were performed by averaging five transverse profiles from each of five non-overlapping regions, with the final value calculated as the mean of these regional averages. MRR was calculated using:

$$MRR = \frac{\Delta V}{\Delta t} = \frac{A_{\mathrm{TIF}} \cdot L}{t} \quad , \qquad (1)$$

where A_{TIF} is the cross-sectional area (μm^2), L is the scan length (μm), and t is the total polishing time (s). To minimize random error and improve model predictive accuracy, a BBD with five center-point replications was used, resulting in 17 experimental runs. The outcomes are presented in Table 2.

Tab. 2　The results of the response surface regression experiments

	AWJP parameters			Output responses	
Run	jet pressure (MPa)	nozzle diameter (mm)	impinging angle (°)	*MRR* (μm^3/s)	*Ra* (nm)
1	2	0.5	30	262.75	0.56
2	4	0.3	45	907.42	1.12
3	3	0.5	45	735.50	0.81
4	3	0.5	45	846.42	0.87
5	2	0.3	45	221.42	0.55
6	3	0.5	45	766.75	0.86
7	3	0.5	45	821.33	0.80
8	4	0.7	45	1873.25	1.22
9	2	0.5	60	208.67	0.71
10	4	0.5	30	1391.92	0.94
11	3	0.3	60	439.33	0.91
12	3	0.3	30	613.08	0.72
13	4	0.5	60	1011.42	1.35
14	3	0.5	45	831.25	0.92
15	2	0.7	45	470.08	0.63
16	3	0.7	60	961.42	0.93
17	3	0.7	30	1304.92	0.78

3　Numerical modeling

3.1　Computational fluid dynamics method

The material removal mechanism of AWJP is inherently complex due to the challenges in directly measuring jet velocity and pressure fields on the workpiece surface. CFD was therefore applied to investigate the microscopic mechanisms and parametric effects of AWJP. Simulation parameters were aligned with experimental conditions, and the Eulerian-Lagrangian approach in the FLUENT software package modeled the multiphase flow of liquid water, air, and abrasive particles. Water and air were treated as Eulerian phases, while abrasive particles were tracked as Lagrangian discrete phases. Besides, key assumptions included negligible nozzle wear during polishing, uniform size and shape of abrasive particles, and constant polishing

slurry concentration throughout the process.

3.2 Simulation analysis of erosion flow field

Velocity contour plots for impinging angles of 30°, 45°, and 60° are presented in Fig. 6 (color online) under a fixed jet pressure of 2 MPa and nozzle diameter of 0.5 mm.

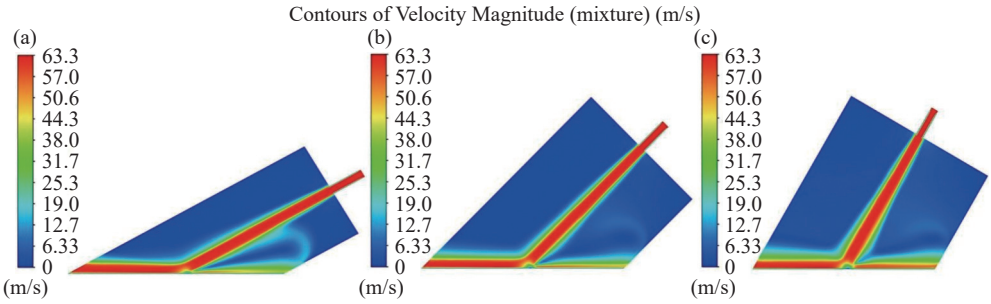

Fig. 6 Velocity cloud plots at different impinging angles. (a) 30°; (b) 45°; (c) 60°

Near-wall velocity distributions, erosion surface pressure profiles, and wall shear stress distributions are shown in Fig. 7 (color online) for the same parametric conditions.

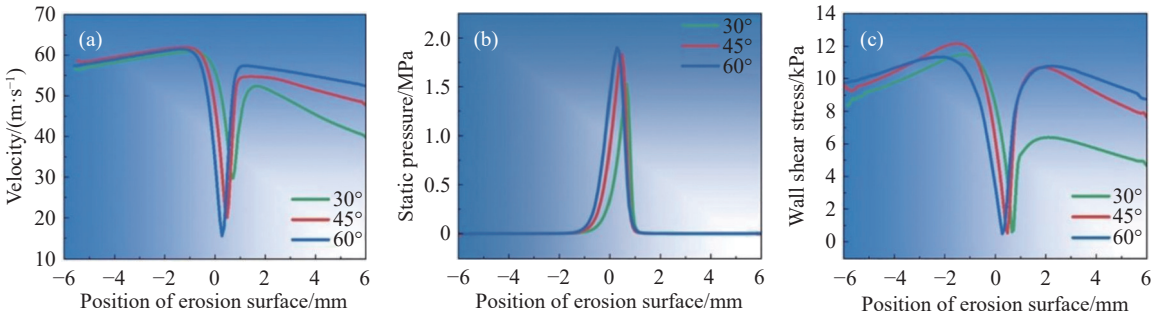

Fig. 7 Simulation curves for different impinging angles. (a) Velocity curve; (b) static pressure curve; (c) wall shear stress curve

These figures reveal asymmetric velocity distributions about the jet axis under oblique incidence, with higher flow velocities observed in the forward direction of the jet. This creates a shear-dominated environment at smaller angles, maximizing lateral particle velocities and material removal efficiency. The velocity stagnation region shifts toward the smaller impinging angle side due to gravitational effects. Increasing the impinging angle reduces the horizontal force component, shifting the material removal mechanism toward vertical impact deformation and potential particle embedding[33–35].

Fig. 8 (color online) presents near-wall velocity distributions, erosion surface pressure profiles, and wall shear stress distributions under jet pressures of 2, 3, and 4 MPa at a fixed impinging angle of 60° and nozzle diameter of 0.5 mm. Increasing jet pressure elevates abrasive particle kinetic energy via Bernoulli's principle, augmenting jet velocity and wall shear stress. The maximum jet velocity increases from 60 m/s at 2 MPa to nearly 90 m/s at 4 MPa, corresponding to a 100% rise in shear stress magnitude. This velocity augmentation enhances micro-cutting efficiency through intensified shear forces. Jet velocity predictions were validated by measuring polishing slurry flow rate at varying pressures using a precision flow meter. Calculated velocities from nozzle diameter and flow rate data showed close agreement with CFD-simulated values, with discrepancies $\leqslant$3% confirming the model's predictive accuracy for AWJP process characterization.

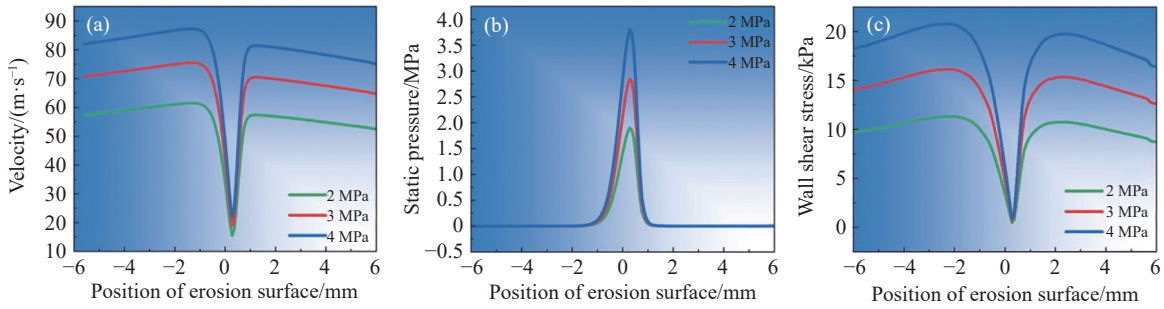

Fig. 8　Simulation curves for different jet pressure. (a) Velocity curve; (b) static pressure curve; (c) wall shear stress curve

Fig. 9 (color online) shows near-wall velocity distributions, erosion surface pressure profiles, and wall shear stress distributions under nozzle diameters of 0.3 mm, 0.5 mm, and 0.7 mm at a fixed impinging angle of 60° and jet pressure of 2 MPa. Larger nozzles expand the jet coverage area due to higher flow rates, with the 0.7 mm diameter yielding the broadest influence zone and highest shear stress. This results from augmented abrasive particle flux, distributing shear forces more uniformly across the workpiece surface and facilitating material removal.

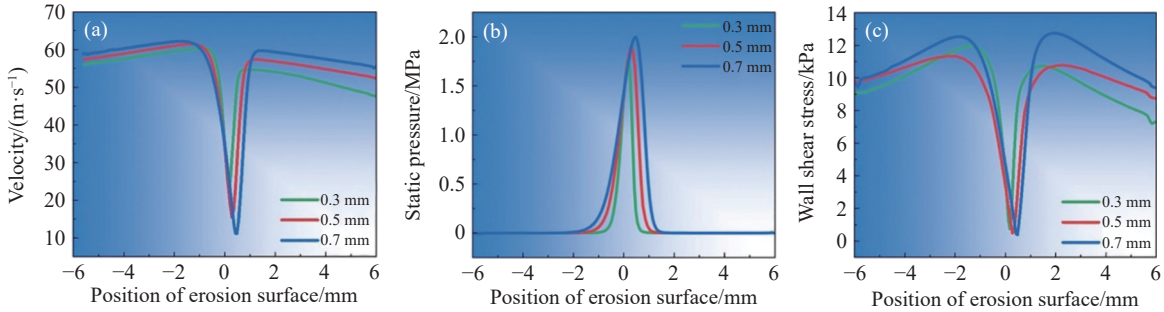

Fig. 9　Simulation curves for different nozzle diameters. (a) Velocity curve; (b) static pressure curve; (c) wall shear stress curve

4　Results and discussion

4.1　Regression model fitting and reliability verification

RSM employs quadratic polynomial regression to model the relationship between experimental responses and independent variables. The canonical form of the regression equation is expressed as:

$$f(x)=\beta_0+\sum_{i=1}^{k}\beta_i x_i+\sum_{i=1}^{k}\beta_{ii}x_i^2+\sum_{i=1}^{k}\beta_{ij}x_i x_j \quad , \quad (2)$$

where $f(x)$ represents the response value, x_i and x_j are independent variable, β_0 is the constant term, β_i is the linear term coefficient, β_{ii} is the quadratic term coefficient, and β_{ij} is the interaction term coefficient.

Based on the experimental results in Table 2, the regression equations for MRR and *Ra* were fitted using Design-Export software:

$$\begin{aligned} MRR = &-992.957\,5+428.835A-2\,769.937\,5B+\\ &39.445C+896.462\,5AB-5.440\,33AC-\\ &14.145\,83BC-21.602\,5A^2+2\,234.875B^2-\\ &0.266\,478C^2 \quad , \end{aligned} \quad (3)$$

$$\begin{aligned} Ra = &0.420\,875-0.184A+0.575B-0.002\,433C+\\ &0.025AB+0.004\,333AC-0.003\,333BC+\\ &0.041\,5A^2-0.337\,5B^2-0.000\,016C^2 \quad , \end{aligned} \quad (4)$$

here A, B, C represent the decision variables of jet pressure, nozzle diameter, and impinging angle respectively.

Residual analysis was conducted on the established regression models. The normal probability dis-

tributions of residuals for MRR and Ra are shown in Fig. 10 (color online). As shown in Fig. 10(a) and 10(b), most sample points are close to a straight line, indicating that both the MRR and Ra regression models have high goodness of fit, verifying the models' reliability.

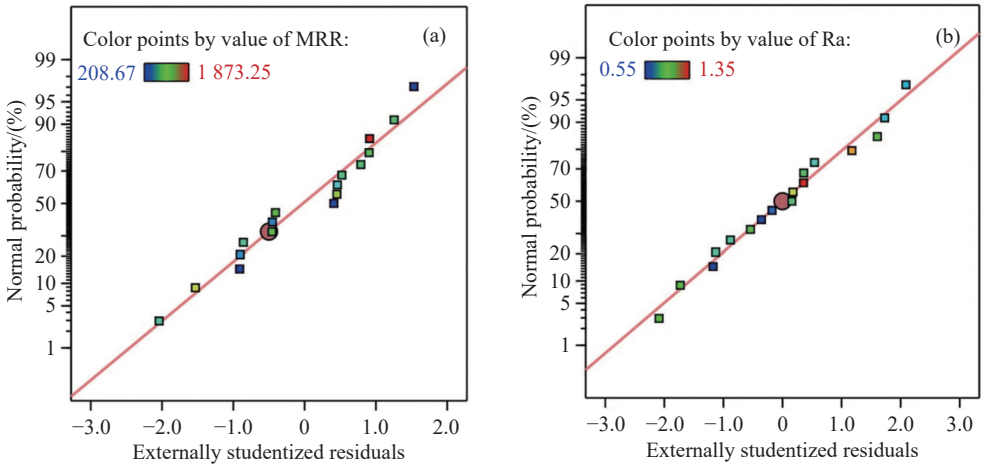

Fig. 10 Normal plots of residuals for (a) MRR and (b) Ra

The analysis of variance (ANOVA) method was employed to evaluate the adequacy and validity of the established regression models, the results are shown in Table 3 and Table 4.

Tab. 3 Analysis of variance for MRR

Source	Sum of squares	Degree of Freedom	Mean square	F-value	P-value	Significance
Model	3.082*e*+06	9	3.425*e*+05	187.33	< 0.000 1	significant
A-jet pressure	2.021*e*+06	1	2.021*e*+06	1 105.56	< 0.000 1	
B-nozzle diameter	7.372*e*+05	1	7.372*e*+05	403.22	< 0.000 1	
C-impinging angle	1.132*e*+05	1	1.132*e*+05	61.95	0.000 1	
AB	1.286*e*+05	1	1.286*e*+05	70.33	< 0.000 1	
AC	26 637.50	1	26 637.50	14.57	0.006 6	
BC	7 203.77	1	7 203.77	3.94	0.087 5	
A^2	1 964.92	1	1 964.92	1.07	0.334 3	
B^2	33 648.28	1	33 648.28	18.41	0.003 6	
C^2	15 136.43	1	15 136.43	8.28	0.023 7	
Residual	12 797.12	7	1 828.16			
Lack of Fit	3 945.28	3	1 315.09	0.594 3	0.651 2	not significant
Pure error	8 851.85	4	2 212.96			
Cor total	3.095e*e*+06	16				

The F-value and the P-value were used to evaluate the statistical significance of the model. MRR and Ra models showed high Fisher's values (187.33 and 29.48, respectively). Low lack of fit F-values (0.594 3 for MRR, 1.37 for Ra) and P-values (0.651 2 for MRR, 0.372 0 for Ra) verified that the experimental data was suitable for constructing predictive models of MRR and Ra[36]. Montgomery indicates that the following conditions should be satisfied during model testing, the F-value > 0.1, the

coefficient of determination $R^2 > 0.95$, the predicted coefficient of determination $R^2_{pred} > 0.7$, the difference between adjusted and predicted determination coefficients < 0.2, coefficient of variation C.V. < 10%, and adequate precision > 4[37]. Based on Table 5, the experiment's reliability and accuracy are validated. The adequate precision values of MRR and Ra models (51.073 and 19.154 7) validate model reliability and signal strength. Both models achieved high R^2 values, indicating strong correlations between predicted and actual responses within the research range.

Tab. 4 Analysis of variance for Ra

Source	Sum of squares	Degree of Freedom	Mean square	F-value	P-value	Significance
Model	0.729 0	9	0.081 0	29.48	< 0.000 1	significant
A-jet pressure	0.594 0	1	0.594 0	216.24	< 0.000 1	
B-nozzle diameter	0.008 4	1	0.008 4	3.08	0.122 9	
C-impinging angle	0.101 2	1	0.101 2	36.86	0.000 5	
AB	0.000 1	1	0.000 1	0.036 4	0.854 1	
AC	0.016 9	1	0.016 9	6.15	0.042 2	
BC	0.000 4	1	0.000 4	0.145 6	0.714 1	
A^2	0.007 3	1	0.007 3	2.64	0.148 3	
B^2	0.000 8	1	0.000 8	0.279 3	0.613 5	
C^2	0.000 1	1	0.000 1	0.018 8	0.894 9	
Residual	0.019 2	7	0.002 7			
Lack of Fit	0.009 8	3	0.003 3	1.37	0.372 0	not significant
Pure error	0.009 5	4	0.002 4			
Cor total	0.748 2	16				

Tab. 5 Fit statistics of ANOVA

	Std.Dev.	Mean	C.V.%	R^2	Adjusted R^2	Predicted R^2	Adeq. Precision
MRR	42.76	803.94	5.32	0.995 9	0.990 5	0.975 1	51.073
Ra	0.052 4	0.863 5	6.07	0.974 3	0.941 3	0.771 7	19.154 7

4.2 Effect of process parameters on MRR and Ra

Perturbation plots were generated using Design-Expert software to evaluate the individual effects of jet pressure, nozzle diameter, and impinging angle on MRR and Ra within the studied ranges. Fig. 11(a) and 11(b) (color online) illustrate the perturbation responses for MRR and Ra, respectively. The steep gradients and curvature in these plots indicate significant parametric influences on surface quality.

The curve *A* of Fig. 11(a) shows that MRR increases with jet pressure, peaking at 4 MPa. This trend aligns with the simulation results of Fig. 8, where higher pressures enhance abrasive velocity, augmenting kinetic energy and shear forces. The velocity-squared relationship explains the MRR enhancement, as higher velocities directly improve micro-cutting efficiency. However, Fig. 11(b) demonstrates that Ra increases concurrently with jet pressure, primarily due to intensified particle embedment and surface micro-cracking. This phenomenon follows contact mechanics principles, where pressures exceeding the material's yield strength induce plastic deformation and brittle fracture, resulting in indentations and cracks.

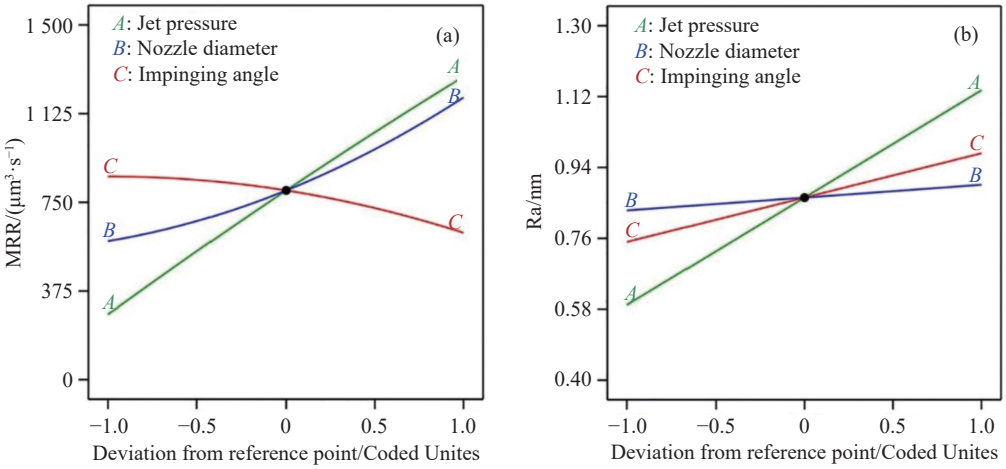

Fig. 11 Perturbation plots obtained from RSM analysis showing the influence of individual process variables on (a) MRR and (b) Ra

Larger nozzle diameters increase jet coverage area, as shown in the simulation results of Fig. 9. This expansion enhances the number of abrasive particles reaching the workpiece surface per unit time, thereby improving material removal capacity. Consequently, MRR increases linearly with nozzle diameter within the studied range, peaking at 0.7 mm, as shown in the curve *B* of Fig. 11(a). Conversely, Fig. 11(b) reveals that Ra remains relatively stable due to uniform shear stress distribution across the expanded jet footprint, thereby minimizing localized surface damage. This behavior aligns with fluid dynamics principles, where increased flow rate maintains abrasive particle concentration while distributing forces homogenously.

The relationship between the impinging angle and the MRR is shown in curve *C* of Fig. 11(a). Within the study range, MRR decreases as the impinging angle increases. Smaller angles correspond to deeper and more extensive material removal. This trend aligns with the simulation results of Fig. 7, where decreasing the impingement angle increases the horizontal velocity component of abrasive particles, augmenting shear forces and micro-cutting efficiency. However, increasing the impinging angle raises Ra due to higher vertical velocity components of abrasive particles, intensifying extrusion deformation and particle embedment. As Fig. 12 (color online) illustrates, small angles facilitate ductile micro-cutting by abrasives, while large angles cause incomplete erosion of surface peaks, leading to cracks and embedded particles.

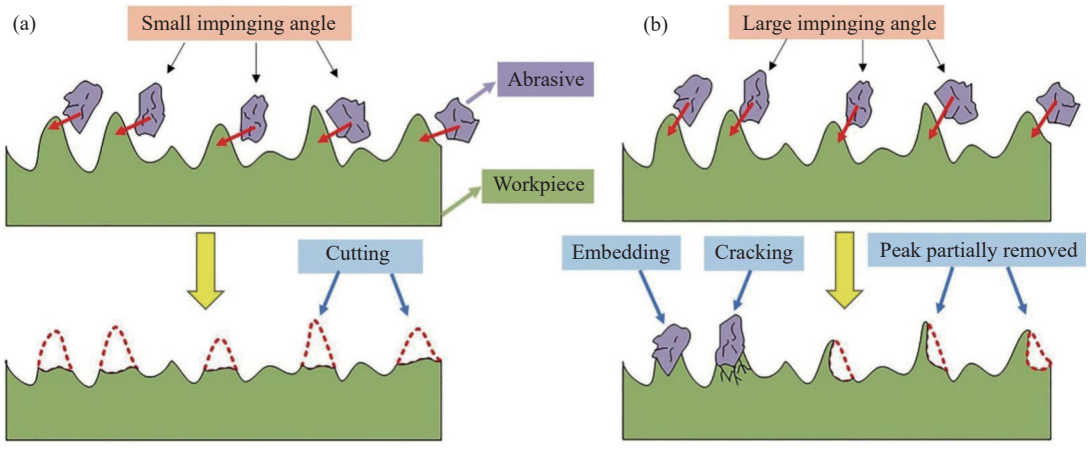

Fig. 12 The material removal process under different jet impinging angles. (a) Small impinging angle; (b) large impinging angle

The 30° angle optimizes the balance between material removal and surface integrity, achieving the highest MRR with acceptable Ra.

4.3 Effect of interaction of process parameters on MRR and Ra

The 3D response surface plots depicting the interactive effects of independent variables on MRR and Ra, derived from experimental results, is shown in Fig. 13 (color online). Table 3 reveals that the P-values of the interaction term *AB* between jet pressure and nozzle diameter, and the interaction term *AC* between jet pressure and impinging angle are both less than 0.01, indicating that these two items have highly significant effects on the MRR regression model. Thus, the effects of *AB* and *AC* on MRR are analyzed using the 3D plots in Fig. 13. As Fig. 13(a) demonstrates, the *AB* interaction exhibits a synergistic effect on MRR: higher jet pressures combined with larger nozzle diameters yield the highest MRR. The optimal point occurs at 4 MPa jet pressure and 0.7 mm nozzle diameter, consistent with single-factor analysis results. When the pressure is low, increasing the diameter will result in an increase in the number of abrasive particles reaching the polishing surface and participating in cutting per unit time, enhancing material removal. However, this diameter increase significantly reduces jet velocity, resulting in limited MRR improvement. Conversely, at small nozzle diameters, increasing pressure significantly increases kinetic energy, leading to substantial MRR gains due to intensified particle impacts.

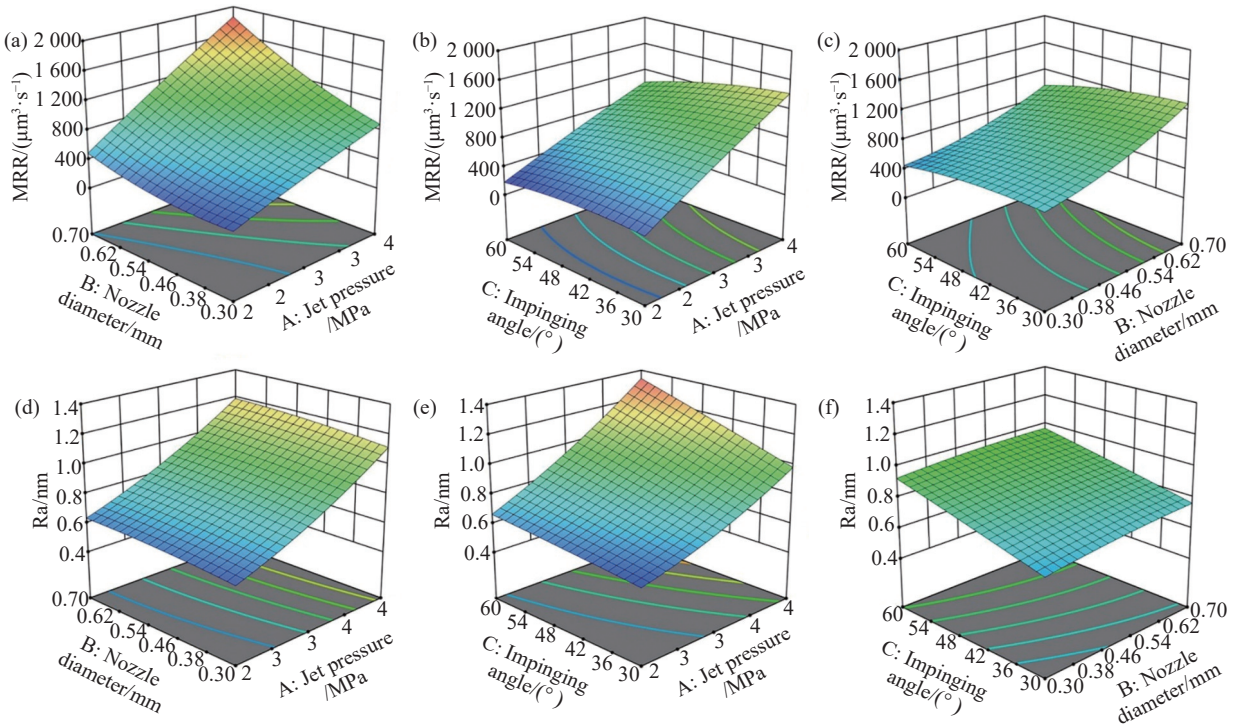

Fig. 13　3D response surface plots depicting the interactions between independent variables and their effect on MRR (a-c) and Ra (d-f)

Fig. 13(b) illustrates the interactive effect of jet pressure and impinging angle on the MRR. The 3D response surface plot presents an overall increasing trend from the lower left to the upper right, indicating that when the jet pressure is higher and the impinging angle is smaller, the polishing removal efficiency is higher, otherwise, it is lower. The maximum MRR can be obtained when jet pressure is 4 MPa and impinging angle is 30°. When the jet pressure is relatively low, reducing the impinging angle will increase the horizontal component of the velocity of the abrasive particles and enhance the

shearing effect on the machining surface. However, weak kinetic energy at low pressures limits MRR improvement despite enhanced micro-cutting. But when the impinging angle is relatively small, increasing the jet pressure will significantly enhance the impact of the jet beam on the machining surface, resulting in a remarkable increase in the MRR.

The analysis of Table 4 reveals that the P-value of the interaction term AC between jet pressure and impinging angle is greater than 0.01 but less than 0.05. Therefore, the impact of AC on the Ra regression model is also remarkable. Fig. 13(e) presents the influence of AC on Ra, showing that lower jet pressures combined with smaller impinging angles yield lower Ra values and superior surface finish. The optimal point occurs at 2 MPa and 30°, where Ra reaches its minimum. At high pressures, reducing the impinging angle increases horizontal shear forces while decreasing vertical impact forces. This mechanism reduces erosion severity by promoting ductile micro-cutting over brittle fracturing, thereby improving surface quality without compromising MRR. Conversely, at large angles, decreasing pressure weakens jet impact, reducing particle embedment and surface cracking.

4.4 Multi-objective process parameter optimization and verification

The GA is a bio-inspired computational model mimicking natural selection and genetic evolution mechanisms[38]. Unlike gradient-based methods, GA employs population-based global search strategies that do not require derivative information or prior domain knowledge. Instead, it relies on fitness evaluation of candidate solutions to iteratively improve performance through crossover, mutation, and selection operations. This characteristic makes GA particularly suitable for complex optimization problems with non-linear and multi-modal objective functions.

In multi-objective optimization problems, each objective function is usually mutually restricted. In general, obtaining a better solution for one objective function will affect the solution of other objective functions. Therefore, the Pareto front is employed to characterize non-dominated solutions. When the AWJP is applied to fused silica, in order to obtain lower Ra, the jet pressure and impinging angle should be decreased. However, this will lead to relatively low MRR and long processing time, which is not conducive to the processing application in actual production. Therefore, the GA is employed for multi-objective optimization, with the MRR and Ra as the objective functions, and jet pressure, nozzle diameter and impinging angle as the decision variables for parameter optimization. Practical process parameter combinations are optimized and selected according to specific machining requirements, balancing surface quality and removal efficiency.

Based on the previously established mathematical models (3) and (4), the MRR and Ra objective functions are formulated as:

$$f(MRR) = -(-992.957\,5 + 428.835A - 2\,769.937\,5B + 39.445C + 896.462\,5AB - 5.440\,33AC - 14.145\,83BC - 21.602\,5A^2 + 2\,234.875B^2 - 0.266\,478C^2)\ , \tag{5}$$

$$f(Ra) = 0.420\,875 - 0.184A + 0.575B - 0.002\,433C + 0.025AB + 0.004\,333AC - 0.003\,333BC + 0.041\,5A^2 - 0.337\,5B^2 - 0.000\,016C^2\ . \tag{6}$$

Using the MATLAB analysis tool for GA iteration, the Pareto optimal solution set is shown in Table 6, and the optimal footprint curve is shown in Fig. 14. The optimal combination of parameters is that the jet pressure is 2 MPa, the nozzle diameter is 0.3 mm, and the impinging angle is 30°. In this situation, the Ra is 0.52 nm and the MRR is 176.86 μm^3/s.

To validate the GA optimization results, the 1st, 8th, and 11th groups were randomly selected from the optimized Pareto solution set in Table 6 for experimental verification, with standoff distance, nozzle feed rate, and abrasive concentration fixed. The relative errors between experimental and pre-

dicted values are presented in Table 7. The Ra errors range from 2.6% to 3.8%, while MRR errors vary between 0.5% and 4.4%. These discrepancies remain within the acceptable range of the actual processing, verifying the reliability of the GA optimization model. The findings demonstrate applicability to homogeneous hard-brittle optical materials, notably various optical glass types, due to their shared mechanical properties.

Tab. 6　Partial Pareto solution set for multi-objective optimization

run	*A*	*B*	*C*	*f*(*MRR*)	*f*(*Ra*)
1	2.00	0.3	30	176.86	0.52
2	2.10	0.3	30	218.77	0.53
3	3.90	0.7	30	1955.06	0.99
4	2.32	0.7	30	743.00	0.64
5	2.00	0.6	30	390.57	0.59
6	2.68	0.7	30	1045.99	0.70
7	3.93	0.7	30	1982.46	1.00
8	2.10	0.7	30	512.08	0.60
9	4.00	0.7	30	2036.53	1.02
10	3.25	0.7	30	1473.19	0.82
11	2.96	0.7	30	1253.51	0.76
12	3.20	0.7	30	1433.27	0.81
…	…	…	…		

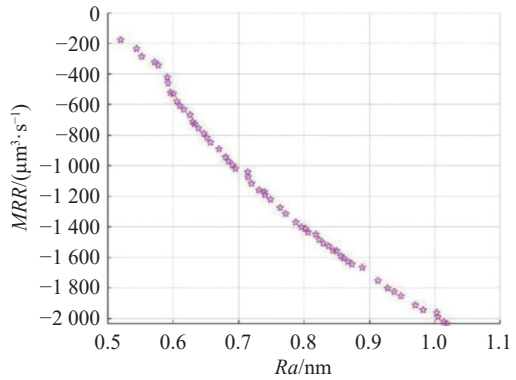

Fig. 14　Pareto footprint diagram of the objective function

Tab. 7　Comparative analysis of experiments

Run	Indicator	Pareto solutions	Experimental value	Error
1	MRR/ (μm³·s⁻¹)	176.86	169.05	4.4%
8		512.08	507.65	0.9%
11		1253.51	1247.25	0.5%
1	Ra/nm	0.52	0.50	3.8%
8		0.60	0.58	3.3%
11		0.76	0.78	2.6%

5　Conclusion

This study systematically integrated CFD simulations and BBD experiments to investigate AWJP of fused silica. CFD simulations indicated that reducing the impinging angle enhanced horizontal abrasive velocity components, promoting micro-cutting effects and improving surface quality. Increasing jet pressure augmented abrasive kinetic energy, thereby strengthening erosive action and MRR. Larger nozzle diameters expanded the jet influence area, increasing abrasive participation in material removal. BBD experiments validated these mechanisms, demonstrating that high-pressure and large-nozzle diameter combinations optimized MRR, while small-impinging angle and low-pressure conditions minimized Ra. GA optimization yielded a parameter combination of 2 MPa jet pressure, 0.3 mm nozzle diameter, and 30° impinging angle, achieving Ra of 0.5 nm and MRR of 169.05 μm³/s with experimental errors of 3.8% (Ra) and 4.4% (MRR). This work establishes a validated framework for optimizing AWJP parameters through the combination of numerical simulations and experiments, which provides assistance for parameter selection in AWJP of complex surfaces and other materials.

References:

[1]　ZHANG H L, LIU H, XU W B, *et al*.. Large aperture diffractive optical telescope: a review[J]. *Optics & Laser Technology*, 2020, 130: 106356.

[2]　WANG H, ZHAO K, SHEN H, *et al*.. Experimental study on direct fabrication of micro channel on fused silica by

picosecond laser[J]. *Journal of Manufacturing Processes*, 2020, 55: 87-95.

[3] RASHEED I A, CHHABRA I M, GUPTA M K, *et al*.. Surface preparation and analysis on fused silica glass substrate with deterministic grinding method[J]. *Materials Today: Proceedings*, 2021, 46: 8239-8247.

[4] ZHAO J, HUANG J F, WANG R, *et al*.. Investigation of the optimal parameters for the surface finish of K9 optical glass using a soft abrasive rotary flow polishing process[J]. *Journal of Manufacturing Processes*, 2020, 49: 26-34.

[5] CAO ZH CH, WANG M, YAN SH Q, *et al*.. Surface integrity and material removal mechanism in fluid jet polishing of optical glass[J]. *Journal of Materials Processing Technology*, 2023, 311: 117798.

[6] CAO ZH CH, WANG M, LIU H T, *et al*.. Modeling and analysis for material removal and surface roughness in fluid jet polishing of optical glass[J]. *Friction*, 2024, 12(7): 1548-1563.

[7] WANG C J, CHEUNG C F, LIU M Y. Numerical modeling and experimentation of three dimensional material removal characteristics in fluid jet polishing[J]. *International Journal of Mechanical Sciences*, 2017, 133: 568-577.

[8] CARON J, BAUMER S. Progress in freeform mirror design for space applications[J]. *Proceedings of SPIE*, 2021, 11852: 118521S.

[9] YANG ZH CH, ZHU L D, ZHANG G X, *et al*.. Review of ultrasonic vibration-assisted machining in advanced materials[J]. *International Journal of Machine Tools and Manufacture*, 2020, 156: 103594.

[10] KUMAR S, TONG ZH, JIANG X Q. Advances in the design and manufacturing of novel freeform optics[J]. *International Journal of Extreme Manufacturing*, 2022, 4(3): 032004.

[11] WAN S L, WEI CH Y, HU CH, *et al*.. Novel magic angle-step state and mechanism for restraining the path ripple of magnetorheological finishing[J]. *International Journal of Machine Tools and Manufacture*, 2021, 161: 103673.

[12] FÄHNLE O W, VAN BRUG H, FRANKENA H J. Fluid jet polishing of optical surfaces[J]. *Applied Optics*, 1998, 37(28): 6771-6773.

[13] FÄHNLE O W. *Shaping and finishing of aspherical optics L surfaces*[D]. Delft: Delft University of Technology, 1998.

[14] FÄHNLE O W, HAUSER K. Abrasive jet polishing approaches to the manufacture of micro-optics with complex shapes[C]. *Optical Fabrication and Testing 2012*, Optica Publishing Group, 2012.

[15] FAEHNLE O, DOETZ M, DAMBON O. Analysis of critical process parameters of ductile mode grinding of brittle materials[J]. *Advanced Optical Technologies*, 2017, 6(5): 349-358.

[16] ZHANG L, DING CH, HAN Y J, *et al*.. Investigation into a novel pulsating cavitation air jet polishing method for Ti-6Al-4V alloy[J]. *Tribology International*, 2022, 175: 107837.

[17] CHEN F J, MIAO X L, TANG Y, *et al*.. A review on recent advances in machining methods based on abrasive jet polishing (AJP)[J]. *The International Journal of Advanced Manufacturing Technology*, 2017, 90(1-4): 785-799.

[18] PAWLUS P, REIZER R, KROLCZYK G M. Modelling and prediction of surface textures after abrasive machining processes: a review[J]. *Measurement*, 2023, 220: 113337.

[19] ZHAO J, GE J Y, KHUDOLEY A, *et al*.. Numerical and experimental investigation on the material removal profile during polishing of inner surfaces using an abrasive rotating jet[J]. *Tribology International*, 2024, 191: 109125.

[20] ZHU H T, HUANG C Z, WANG J, *et al*.. Experimental study on abrasive waterjet polishing for hard–brittle materials[J]. *International Journal of Machine Tools and Manufacture*, 2009, 49(7-8): 569-578.

[21] MATSUMURA T, MURAMATSU T, FUEKI S. Abrasive water jet machining of glass with stagnation effect[J]. *CIRP Annals*, 2011, 60(1): 355-358.

[22] LI Z Z, WANG J M, PENG X Q, *et al*.. Removal of single point diamond-turning marks by abrasive jet polishing[J]. *Applied Optics*, 2011, 50(16): 2458-2463.

[23] TSAI F C, YAN B H, KUAN C Y, *et al*.. A Taguchi and experimental investigation into the optimal processing conditions for the abrasive jet polishing of SKD61 mold steel[J]. *International Journal of Machine Tools and Manufacture*, 2008, 48(7-8): 932-945.

[24] WANG C J, CHEUNG C F, HO L T, *et al*.. A novel multi-jet polishing process and tool for high-efficiency polishing[J]. *International Journal of Machine Tools and Manufacture*, 2017, 115: 60-73.

[25] KUMARAN S T, KO T J, UTHAYAKUMAR M, *et al*.. Prediction of surface roughness in abrasive water jet machining of CFRP composites using regression analysis[J]. *Journal of Alloys and Compounds*, 2017, 724: 1037-1045.

[26] CAO ZH CH, CHEUNG B C F, KONG L B. Computational fluid dynamics–based analysis of material removal characteristics in fluid jet polishing[J]. *Proceedings of the Institution of Mechanical Engineers, Part B: Journal of*

Engineering Manufacture, 2016, 230(6): 1035-1048.

[27] ZHANG Z L, CHEUNG C F, GUO J, *et al*.. Pressure-dependent material removal rate model of fluid jet polishing[J]. *International Journal of Mechanical Sciences*, 2024, 281: 109517.

[28] YANG Y Y, YANG M, LI CH H, *et al*.. Machinability of ultrasonic vibration-assisted micro-grinding in biological bone using nanolubricant[J]. *Frontiers of Mechanical Engineering*, 2023, 18(1): 1.

[29] XIA Z B, FANG F ZH, AHEARNE E, *et al*.. Advances in polishing of optical freeform surfaces: a review[J]. *Journal of Materials Processing Technology*, 2020, 286: 116828.

[30] LI J H, MA W H, HOU X. Modeling and experiment on elastic material removal in nanoparticle jet polishing[J]. *Journal of Manufacturing Processes*, 2024, 120: 317-336.

[31] CHEUNG C F, WANG C J, CAO Z C, *et al*.. Development of a multi-jet polishing process for inner surface finishing[J]. *Precision Engineering*, 2018, 52: 112-121.

[32] ZHANG X P, YAO P, ZHOU P F, *et al*.. Removal mechanism and grinding performance of ZTA nanocomposite ceramics using ternary-hybrid nanofluid minimum quantity lubrication technology[J]. *Journal of Manufacturing Processes*, 2024, 132: 1-13.

[33] QU SH SH, YAO P, GONG Y D, *et al*.. Environmentally friendly grinding of C/SiCs using carbon nanofluid minimum quantity lubrication technology[J]. *Journal of Cleaner Production*, 2022, 366: 132898.

[34] QU SH SH, WEI CH X, YANG Y Y, *et al*.. Grinding mechanism and surface quality evaluation strategy of single crystal 4H-SiC[J]. *Tribology International*, 2024, 194: 109515.

[35] QU SH SH, YAO P, GONG Y D, *et al*.. Modelling and grinding characteristics of unidirectional C-SiCs[J]. *Ceramics International*, 2022, 48(6): 8314-8324.

[36] GREENLAND S, SENN S J, ROTHMAN K J, *et al*.. Statistical tests, *P* values, confidence intervals, and power: a guide to misinterpretations[J]. *European Journal of Epidemiology*, 2016, 31(4): 337-350.

[37] MONTGOMERY D C. *Design and Analysis of Experiments*[M]. 2nd ed. Hoboken: John Wiley & Sons, 1983.

[38] AMUTHA J, SHARMA S, SHARMA S K. Strategies based on various aspects of clustering in wireless sensor networks using classical, optimization and machine learning techniques: review, taxonomy, research findings, challenges and future directions[J]. *Computer Science Review*, 2021, 40: 100376.

Author Biography:

YAO Peng (1979—), male, born in Dalian, Liaoning Province, PhD, Professor, Doctoral Supervisor. He received his doctoral degree from Northeastern University (Japan) in 2011, mainly engaged in research on grinding and ultra precision machining technology, multi energy field composite precision machining technology, and laser micro/nano machining technology. E-mail: yaopeng@sdu.edu.cn